PCCP

PAPER

View Article Online
View Journal | View Issue

Cite this: *Phys. Chem. Chem. Phys.*, 2025, **27**, 14630

Hydroxy-substituted aromatic N-heterocycles as high-affinity CO_2 adsorbents: a DFT study†

Puthiyavalappil K. Arathi[ab] and Cherumuttathu H. Suresh *[abc]

Hydroxy-substituted aromatic N-heterocycles, including hydroxy pyridine (py), dihydroxy naphthyridines (nt), and trihydroxy pyridonaphthyridines (pn), have been investigated for their potential as CO_2 adsorbents using density functional theory (DFT) calculations. Building on the pioneering work of Luo *et al.*, who demonstrated exceptional CO_2 capture capacities in pyridine-containing anion-functionalized ionic liquids, this study extends the exploration to a broader range of N-heterocycles. These N-heterocycles exhibit exceptional CO_2 capture capabilities, driven by cooperative interactions between nitrogen and oxygen centres with CO_2. The adsorption capacity increases with the number of nitrogen centres and hydroxy groups, with py, nt, and pn systems binding one, two, and three CO_2 molecules, respectively. Notably, anionic N-heterocycles exhibit dramatically improved CO_2 adsorption compared to their neutral counterparts, forming covalent bonds with CO_2. The presence of counter cations, such as lithium or tetramethylphosphonium ions, further stabilizes CO_2 adsorption, resulting in shorter interaction distances and higher exergonic free energy values. Solvent effects modeled using monoethanolamine (MEA) indicate a modest reduction in interaction energies for neutral and anionic systems, while ion-paired systems exhibit enhanced CO_2 affinity in solution. Additionally, molecular electrostatic potential (MESP) analysis highlights the key adsorption sites and charge delocalization mechanisms that facilitate CO_2 capture. The study also finds that enol–keto transformations, which could lead to CO_2 conversion into carboxylates, are energetically unfavorable due to the loss of aromatic stability. These findings underscore the potential of hydroxy-substituted N-heterocycles, particularly in their anionic and cation-stabilized forms, as promising candidates for efficient CO_2 capture. The insights gained from this study provide valuable guidelines for the design of next-generation CO_2 sequestration materials and highlight new directions for experimental validation and real-world applications.

Received 19th March 2025,
Accepted 20th June 2025

DOI: 10.1039/d5cp01075f

rsc.li/pccp

Introduction

The rising levels of atmospheric CO_2 have driven global efforts to develop efficient capture and conversion strategies.[1–7] Traditional methods, such as sequestration and storage face significant challenges related to cost, efficiency, and environmental impact.[8–10] In contrast, adsorption-based techniques employing nitrogen-rich molecules and materials present a promising alternative due to their operational simplicity and lower energy demands.[11–15]

Ionic liquids (ILs) have gained attention as versatile media for both CO_2 capture and conversion. The evolution of ILs, from conventional to amine-functionalized and multi-sited ILs, has led to remarkable improvements in CO_2 absorption efficiency.[16–27] Among these advancements, the work by Luo *et al.* stands out as a significant contribution to the field. In their seminal study, Luo *et al.* demonstrated that pyridine-containing anion-functionalized ionic liquids exhibit exceptional CO_2 capture capacities, achieving up to 1.60 mol CO_2 per mol IL through multiple-site cooperative interactions.[28] Their work revealed that the presence of nitrogen and oxygen atoms in the anion, along with π-electron delocalization in the pyridine ring, significantly enhances CO_2 binding. This cooperative interaction between the electronegative oxygen and nitrogen atoms in the anion and CO_2 was shown to be the key driver of the high CO_2 capture capacity.[28]

[a] *Chemical Sciences and Technology Division, CSIR-National Institute for Interdisciplinary Science and Technology, Thiruvananthapuram, 695019, India. E-mail: sureshch@gmail.com*
[b] *Academy of Scientific and Innovative Research (AcSIR), Ghaziabad, 201002, India*
[c] *Srinivasa Ramanujan Institute for Basic Sciences, Kerala State Council for Science, Technology and Environment, Kottayam, Kerala 686501, India*

† Electronic supplementary information (ESI) available: SCF energies, zero-point correction, thermal correction to Gibbs, free energies and BSSE (Table S1), relative interaction energies of all complexes (Table S7), Rrelative free energies of all complexes (Table S8), Ssolvation energies of anion (Table S11), Ssolvation energies of anions in presence of counter cation (Table S12) and Cartesian coordinates of all the systems (Table S17). See DOI: **https://doi.org/10.1039/d5cp01075f**

Building on the insights from Luo *et al.*,[28] this study aims to further explore the potential of hydroxy-substituted aromatic N-heterocycles as high-affinity CO_2 adsorbents. While Luo *et al.* focused on the role of pyridine-containing ILs, we extend this approach to investigate a broader range of N-heterocycles, including hydroxy pyridines (py), dihydroxy naphthyridines (nt), and trihydroxy pyridonaphthyridines (pn), to understand how the strategic incorporation of nitrogen and hydroxy groups within these molecular structures can enhance CO_2 capture through cooperative binding mechanisms.

Recent studies have highlighted the significance of multiple-site cooperative interactions in enhancing CO_2 capture.[28–38] Inspired by Luo *et al.*'s findings,[28] we hypothesize that the presence of multiple nitrogen and hydroxy groups in these N-heterocycles will lead to enhanced CO_2 capture through similar cooperative interactions. Specifically, we aim to elucidate the electronic and structural factors governing CO_2 interaction and conversion in these systems, providing valuable insights for the design of efficient CO_2 capture materials.

This study will assess the CO_2 capture capacity of neutral and anionic forms of these molecules, identify the preferred binding sites for CO_2, investigate the thermodynamics of CO_2 capture and conversion processes, explore the influence of molecular structure, charge and counter cation on CO_2 interaction and conversion efficiency. By unravelling the intricate relationship between molecular structure, charge, and CO_2 capture capabilities, this study aims to contribute to the development of innovative solutions for mitigating the environmental impact of greenhouse gas emissions.

In this study, we focus on the adsorption of CO_2 onto functionalized organic molecules, rather than its absorption into bulk liquid or solid phases. Adsorption refers to surface-level binding at active sites, whereas absorption involves uptake into the bulk. The molecules studied here are potential precursors for integration into extended frameworks such as MOFs or ZIFs, or for surface immobilization on porous substrates to enhance CO_2 capture.[8] For clarity, the term adsorption is used throughout this work to describe CO_2 binding to molecular surface.

Effective CO_2 capture requires optimizing adsorption energy and viscosity. A moderate adsorption energy (*e.g.*, -5 to -10 kcal mol^{-1}) is often ideal-it indicates sufficiently strong binding for efficient capture but also reversible desorption, enabling regeneration.[39] Viscosity also influences capture performance, as lower viscosity improves mass transfer. Nitrogen-functionalized molecules, as explored in this study, offer an advantageous balance of moderate binding strength and favourable rheological properties, making them promising candidates for efficient CO_2 adsorption.[40,41]

Methodology and molecular design strategies

All geometry optimizations were performed using density functional theory (DFT) at the M06-2X/6-311++G(d,p) level, as implemented in the Gaussian 16 suite of programs.[42] The inclusion of diffuse functions in the basis set was essential for accurately describing the electronic structure of anionic complexes. All optimized geometries were confirmed to have only real vibrational frequencies, ensuring they represent true minima on the potential energy surface, while transition states exhibited a single imaginary frequency, validating their nature as first-order saddle points. The M06-2X functional is well-regarded for its accuracy in modelling intermolecular non-covalent interactions, crucial in understanding CO_2-adsorbent complexes.[43] To identify the most stable equilibrium structures, various initial guess geometries were considered, placing CO_2 near electron-rich sites of the adsorbent. The lowest energy structures from these optimizations were used for further analysis. The adsorption energy (ΔE_{ad}) of CO_2 was calculated using the supermolecule approach as follows (eqn (1)):

$$\Delta E_{ad} = E_{complex} - (E_{adsorbent} + E_{CO_2}) + E_{BSSE} \quad (1)$$

Here, $E_{complex}$, $E_{adsorbent}$, E_{CO_2} are the zero-point energy (ZPE)-corrected total energies of the complex, the isolated N-heterocycle (Nhet) and CO_2, respectively (Unless stated otherwise, all energies reported hereafter include ZPE corrections). The basis set superposition error (E_{BSSE}), was evaluated using the counterpoise correction method of Boys and Bernardi[44] to account for artificial stabilization arising from basis set overlap. To account for solvent effects, which significantly influence chemical reactivity, selectivity, and product stability,[45] single-point energy calculations were performed at the M06-2X/6-311++G(d,p) level using the gas-phase optimized geometries. Solvation by monoethanolamine (MEA), a commonly used amine-based solvent in post-combustion CO_2 capture systems, was modeled using the SMD (solvation model based on density) approach within the self-consistent reaction field (SCRF) framework.[46,47] MEA was chosen not to model absorption into the solvent itself but to serve as a reference medium, enabling a comparative assessment of the CO_2 adsorption performance of the N-heterocyclic systems relative to a well-established industrial benchmark.

In addition to adsorption energies (ΔE_{ad}), Gibbs free energies of adsorption (ΔG_{ad}) were computed to offer a more complete thermodynamic perspective. These calculations were performed in the gas phase at 293 K and 1 atm, consistent with ambient CO_2 capture conditions.

To further elucidate electronic features relevant to CO_2 binding, topological analysis of the molecular electrostatic potential (MESP), $V(\mathbf{r})$, was carried out. The MESP as defined in eqn (2) was computed at the M06-2X/6-311++G(d,p) level for all optimized geometries using Gaussian 16. This analysis identifies electron-rich regions such as lone pairs and π-systems – critical for understanding interaction sites in the hydroxy-substituted N-heterocycles, their anionic counterparts, and the corresponding CO_2 complexes.

$$V(\mathbf{r}) = \sum_{A}^{N} \frac{Z_A}{|\mathbf{r} - \mathbf{R}_A|} - \int \frac{\rho(\mathbf{r}')\mathrm{d}^3\mathbf{r}'}{|\mathbf{r} - \mathbf{r}'|} \quad (2)$$

In eqn (2), $\rho(\mathbf{r}')$ is the electron density, Z_A is the charge on nucleus A located at $\mathbf{R}_A$, and $\mathbf{r}'$ is a dummy integration variable.[48,49] The MESP value at a (3, +3) critical point observed in electron rich regions such as lone pairs and π-bonds in topology analysis is called V_{min}. The V_{min} analysis is useful to understand the subtle variations and delocalization in electron density distribution due to the interactive behaviour of molecules.[49–52]

The molecular design strategy focuses on how introducing nitrogen and oxygen atoms affects the CO_2 capture capacity of N-heterocycle. To explore this, we studied a series of hydroxy-substituted molecules – pyridine (py), naphthyridine (nt) and pyridonaphthyridine (pn) – featuring both two- and three-membered rings with systematically increasing numbers of carbon, nitrogen, and oxygen atoms. This enables evaluation of enhanced cooperative interactions due to the increased number of potential CO_2 binding sites.

The choice of these molecular systems is grounded in prior research: hydroxy pyridines (py) have been examined for CO_2 adsorption, notably by Luo *et al.* in the context of ionic liquids.[28] While naphthyridines (nt) have been extensively studied for their pharmacological properties,[53–57] their potential for CO_2 capture remains largely unexplored. Similarly, some pyridonaphthyridine derivatives have shown therapeutic promise,[58,59] but their abilities for CO_2 adsorption have not been thoroughly investigated.

Additionally, the study extends to anionic forms of hydroxy-N-heterocycles (deprotonated form) to assess the impact of electron density on CO_2 binding.[60–76] We analyze how electron distribution evolves with the addition of aromatic rings and heteroatoms as the molecules transition from monoanionic to dianionic and trianionic states.

By combining the molecular design strategies with DFT calculations and MESP analysis,[50–52,77,78] this study aims to provide a comprehensive understanding of the structure–activity relationships governing CO_2 capture and conversion in these systems.

Results and discussion

N-Heterocycles and CO_2 complexes

The chemical structure of hydroxy pyridine (py), the selected set of dihydroxy naphthyridines (nt to nt12), and the set of trihydroxy pyridonaphthyridines (pn1 to pn36) are presented in Fig. 1 (see ESI† for their IUPAC names, Fig. S1). Collectively, these compounds are referred to as N-heterocycles (Nhet). In all Nhet systems, the hydroxy groups are strategically positioned adjacent to nitrogen atoms to maximize the potential for synergistic interactions with CO_2. This design rationale is based on calculated adsorption energies (ΔE_{ad}) for positional isomers of hydroxypyridine: 2-hydroxypyridine showed the most favourable interaction energy (-11.3 kcal mol^{-1}), compared to -10.3 kcal mol^{-1} for 3-hydroxypyridine and -10.4 kcal mol^{-1} for 4-hydroxypyridine. The enhanced performance of 2-hydroxypyridine is attributed to cooperative binding between the adjacent nitrogen and hydroxyl functionalities, which strengthens both the N···CO_2 and O–H···OCO interactions.

The minimum energy structures for each Nhet compound were identified, along with stable configurations of their CO_2 complexes, denoted as Nhet···$(CO_2)_n$ complexes, where n = 1 for py, n = 1 and 2 for nt and n = 1, 2, and 3 for pn systems. The relative energy of each structural isomers of nt and pn (ΔE_{rel}) was calculated using the equation (eqn (3)):

$$\Delta E_{rel} = E_{sample} - E_{standard} \quad (3)$$

where E_{sample} is the energy of the isomer under consideration, and $E_{standard}$ is the energy of the most stable isomer. By this convention, the most stable isomer has ΔE_{rel} = 0.0 kcal mol^{-1}, and positive values denote less stable structures (Table 1 and 2).

The Nhet···CO_2 complex is characterized by two key interactions: the nitrogen-to-carbon (N···CO_2) interaction and the CO_2 oxygen-to-hydroxy hydrogen (CO_2···HO) interaction. The N···CO_2 interaction enhances electron density at the oxygen atoms of CO_2, thereby strengthening the CO_2···HO interaction. This synergistic effect results in positive cooperativity, where an improvement in N···CO_2 interaction leads to enhanced CO_2···HO interaction. Consequently, the CO_2 adsorption efficiency of Nhet can be attributed to the combined influence of these mutually reinforcing interactions.

MESP analysis of N-heterocycles and CO_2 complexes

Molecular electrostatic potential (MESP) topology analysis uses the minimum electrostatic potential (V_{min}) to map lone pair electron density around relevant atoms.[52] As illustrated in Fig. 1, nitrogen centres in Nhet are identified based on their V_{min} values and are numbered in decreasing order of magnitude, with N1 being the most electron rich, followed by N2 and N3. These nitrogen atoms serve as the primary interaction sites for CO_2.

The V_{min} distribution of a representative set of Nhet systems is shown in Fig. 2. In py, the V_{min} value for the nitrogen lone pair is -47.9 kcal mol^{-1}. Among nt systems, nt1 exhibits the most negative V_{min} (-53.1 kcal mol^{-1}) while nt12, with a V_{min} -40.1 kcal mol^{-1}, comparatively less electron-dense. The V_{min} values of N1 and N2 within the same nt molecule show minimal variation, with an average difference of approximately 10 kcal mol^{-1}. In pn systems, V_{min} varies significantly across N1, N2 and N3, ranging from -53.1 to -31.3 kcal mol^{-1}, depending on the position of nitrogen centres (Table S2, ESI†). Based on the MESP analysis, nitrogen centres are identified as the most probable sites for CO_2 interaction. The affinity of CO_2 for different nitrogen centres follows a general trend, where a more negative V_{min} corresponds to stronger interaction potential. MESP plotted on 0.005 a.u. isodensity surface provides a visual representation of electron reorganization during CO_2 complexation with N-heterocycles (Fig. 3).[79] When the carbon atom of CO_2 accepts electron density from the nitrogen centre of Nhet, a counterbalancing electron density donation occurs from the oxygen of CO_2 to the hydroxy hydrogen of Nhet. This process leads to delocalization of electron density around the lone pairs of nitrogen and oxygen atoms due to the N···CO_2

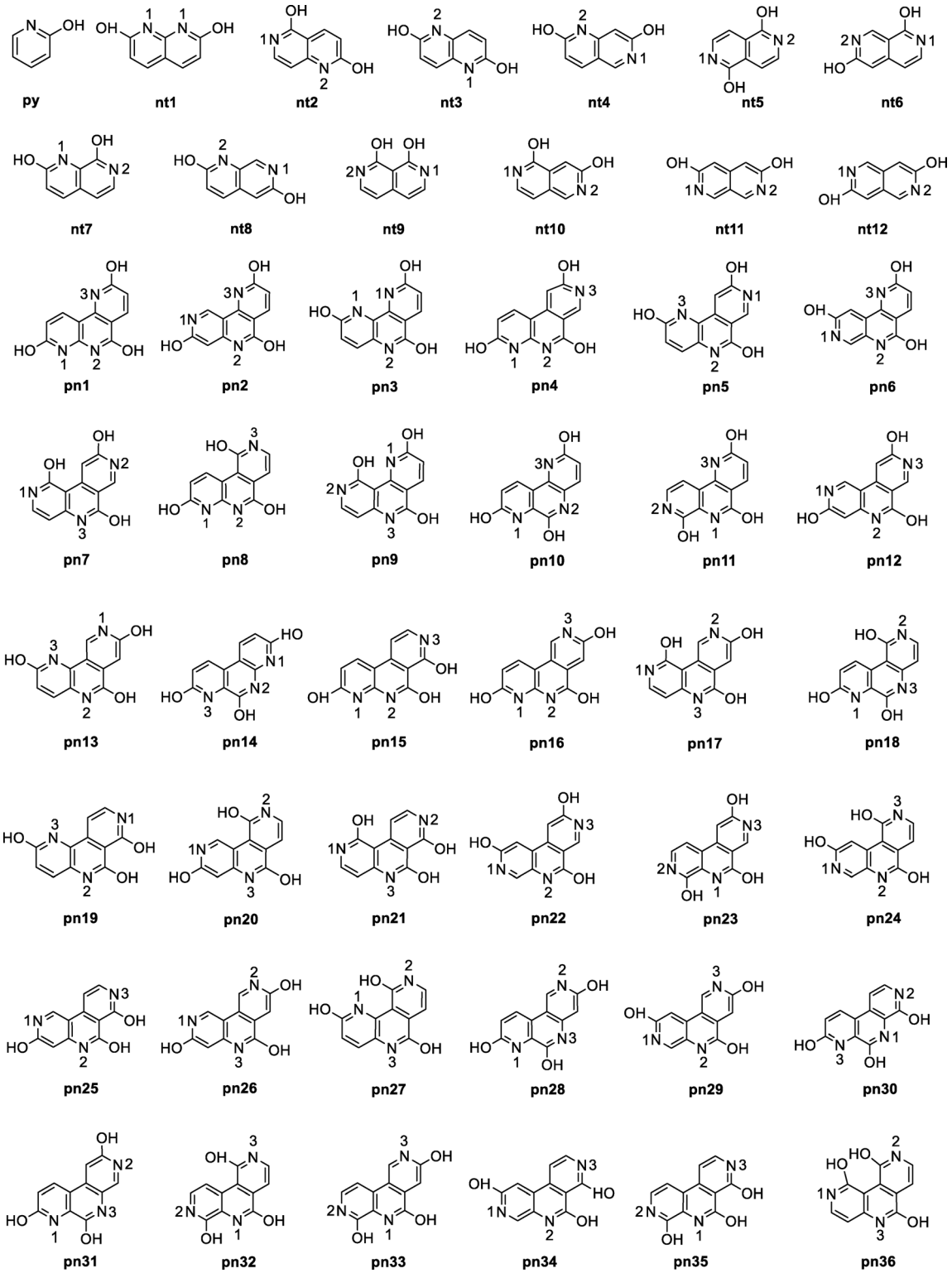

Fig. 1 Chemical structures of hydroxy pyridine (py), 12 dihydroxy naphthyridines (nt), and 36 trihydroxy pyridonaphthyridines (pn).

and $CO_2\cdots HO$ interactions. Because of the mutually compensating effect of these interactions, apart from the noncovalently bonded regions, the overall electron distribution in the Nhet$\cdots CO_2$ complex remains largely unchanged outside the noncovalently bonded regions. For instance, in pn systems, the oxygen atoms of hydroxy groups exhibit only minor changes in V_{min} even with successive CO_2 adsorption. Similarly, nitrogen atoms not directly involved in noncovalent bonding retain nearly the same V_{min} values in Nhet$\cdots CO_2$ and Nhet$\cdots(CO_2)_2$ complexes. This consistency suggests a steady interaction energy

Table 1 V_{min}, ΔE_{rel}, BSSE corrected ΔE_{ad} and ΔG_{ad} values of dihydroxy naphthyridines at M06-2X/6-311++G(d,p) level of theory. All values in kcal mol^{-1}

	V_{min}						
Molecules	N1	N2	ΔE_{rel}	ΔE_{ad1}	ΔE_{ad2}	ΔG_{ad1}	ΔG_{ad2}
nt1	−53.1	−53.1	0.0	−10.5	−10.7	−3.7	−2.7
nt2	−47.0	−42.8	0.5	−10.9	−10.1	−3.1	−3.7
nt3	−43.3	−43.2	1.5	−10.5	−10.0	−3.4	−3.5
nt4	−43.8	−43.7	2.9	−10.7	−10.1	−3.6	−3.6
nt5	−44.0	−43.9	3.5	−10.8	−10.3	−3.9	−3.4
nt6	−44.5	−42.4	4.0	−11.0	−10.1	−3.8	−3.4
nt7	−51.4	−47.6	5.1	−10.2	−10.1	−3.9	−3.6
nt8	−44.5	−42.0	5.5	−10.6	−9.9	−3.6	−3.7
nt9	−45.2	−44.9	6.1	−10.8	−10.3	−3.4	−3.4
nt10	−44.2	−40.9	6.5	−10.8	−10.0	−3.7	−3.4
nt11	−41.2	−41.0	6.5	−10.6	−10.2	−3.7	−3.6
nt12	−40.2	−40.1	10.3	−10.5	−10.0	−3.8	−3.7

Table 2 ΔE_{rel}, BSSE corrected ΔE_{ad} and ΔG_{ad} values of trihydroxy pyridonaphthyridines at M06-2X/6-311++G(d,p) level of theory. All values in kcal mol^{-1}

Molecules	ΔE_{rel}	ΔE_{ad1}	ΔE_{ad2}	ΔE_{ad3}	ΔG_{ad1}	ΔG_{ad2}	ΔG_{ad3}
pn1	0.0	−10.5	−10.8	−6.4	−4.1	−2.0	−3.1
pn2	2.5	−10.8	−10.2	−8.1	−3.1	−3.8	−3.0
pn3	4.2	−11.6	−6.3	−9.4	−4.5	−3.2	−2.4
pn4	4.7	−10.5	−10.8	−9.0	−1.7	−3.8	−4.7
pn5	4.7	−10.5	−10.2	−7.9	−1.7	−5.0	−3.4
pn6	5.0	−10.6	−10.0	−7.8	−3.0	−1.9	−2.1
pn7	5.2	−10.8	−10.0	−9.6	−3.2	−3.7	−3.5
pn8	5.2	−10.5	−10.7	−9.1	−3.3	−3.7	−3.6
pn9	5.3	−10.8	−10.9	−9.0	−3.2	−3.6	−3.5
pn10	5.5	−10.2	−9.2	−7.8	−2.0	−4.9	−3.5
pn11	5.7	−9.9	−10.7	−6.2	−1.9	−5.1	−0.9
pn12	6.2	−10.8	−10.1	−9.4	−3.5	−3.7	−3.6
pn13	6.4	−10.5	−10.1	−8.2	−3.6	−3.7	−3.5
pn14	6.6	−10.5	−10.6	−8.6	−3.4	−3.7	−3.6
pn15	6.9	−10.5	−10.5	−9.0	−3.4	−3.7	−3.5
pn16	7.4	−10.5	−10.7	−9.0	−3.7	−3.6	−1.8
pn17	7.5	−10.9	−10.0	−9.5	−3.8	−3.4	−3.6
pn18	7.8	−9.7	−10.8	−9.2	−3.7	−3.7	−3.5
pn19	8.0	−10.6	−9.8	−6.7	−3.7	−3.5	−3.7
pn20	8.0	−10.7	−10.1	−9.4	−3.7	−3.6	−3.6
pn21	8.8	−10.9	−10.1	−9.2	−3.7	−3.7	−2.0
pn22	8.9	−10.6	−9.9	−9.4	−3.8	−3.7	−3.3
pn23	9.0	−10.4	−10.0	−9.2	−3.7	−3.6	−3.5
pn24	9.2	−10.6	−9.8	−9.5	−3.7	−3.5	−3.4
pn25	9.4	−10.8	−9.8	−9.5	−3.6	−3.5	−3.4
pn26	9.6	−10.8	−10.0	−9.4	−3.8	−3.5	−3.5
pn27	9.7	−10.6	−10.9	−7.2	−3.6	−3.5	−0.4
pn28	9.7	−9.7	−10.3	−9.8	−3.5	−3.9	−1.7
pn29	9.8	−10.6	−9.8	−9.4	−3.4	−3.7	−1.5
pn30	10.0	−10.3	−10.0	−8.9	−3.5	−3.5	−3.1
pn31	10.2	−9.8	−10.0	−9.6	−4.9	−1.0	−3.7
pn32	10.3	−9.9	−10.6	−9.4	−3.9	−2.5	−2.1
pn33	10.9	−10.3	−10.0	−9.3	−3.8	−2.6	−3.4
pn34	12.4	−10.5	−9.6	−9.4	−4.2	−2.1	−3.5
pn35	12.6	−10.3	−9.9	−9.2	−3.8	−2.5	−3.6
pn36	15.5	−10.8	−10.1	−9.5	−4.0	−2.2	−3.8

value for CO_2 adsorption, allowing Nhet to effectively capture up to three CO_2 molecules.

Transition state (TS) calculations

To further understand the CO_2 capture process, transition state (TS) calculations were performed to evaluate the activation

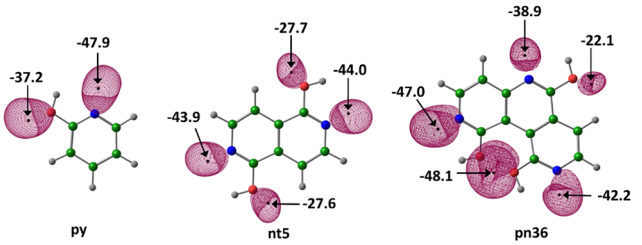

Fig. 2 MESP topography of representative cases of py, nt and pn system at M06-2X/6-311++G(d,p) level of theory. The black dots represent V_{min} positions. MESP isosurface value at −12 kcal mol^{-1}. All values in kcal mol^{-1}. (Color key: green-C, grey-H, blue-N, red-O).

energies for the reaction pathways involving different CO_2 binding configurations. For the py system, the transition state for the first CO_2 binding (TS1) is located at −0.7 kcal mol^{-1}, with the corresponding acid formation at −2.9 kcal mol^{-1}. In the case of nt5, the activation energy for CO_2 binding decreases as additional CO_2 molecules are added, with values of −1.3 kcal mol^{-1} for the first binding, −5.0 kcal mol^{-1} for the diacid formation (TS2). The pn36 system exhibits a similar trend, with transition state energies of −2.2 kcal mol^{-1} for TS1 and −5.1 kcal mol^{-1} for TS2, with a significant drop in activation energy observed at −0.9 kcal mol^{-1} for the triacid formation (TS3). These calculations provide valuable insight into the energetic barriers for CO_2 binding and highlight the influence of molecular structure on the activation energies and stability of the intermediates.

CO_2 adsorption and enol–keto transformation in N-heterocycles

The nitrogen-to-carbon interaction distance (d_{NC}) serves as an initial indicator of interaction strength. Notably, all captured CO_2 molecules bind to the nitrogen centre at distances ranging from 2.70 to 2.90 Å. The complexes are further stabilized by $CO_2\cdots HO$ hydrogen bonding, with hydrogen bond distance (d_{OH}) ranging from 1.98 to 2.12 Å (Table S3, ESI†). Representative examples of Nhet$\cdots(CO_2)_n$ complexes are illustrated in Fig. 4. The noncovalent interactions slightly reduce the OCO bond angle from 180°.

The py$\cdots CO_2$ complex demonstrates an interaction energy (ΔE_{ad}) of −10.8 kcal mol^{-1}, with a corresponding free energy of interaction (ΔG_{ad}) of −3.8 kcal mol^{-1}, confirming its exergonic nature. For nt systems, ΔE_{ad1} represents the reaction nt + CO_2 → nt$\cdots CO_2$, corresponding to CO_2 adsorption at the N1 site. Similarly, ΔE_{ad2} refers to the energy released upon CO_2 adsorption at the N2 site of the nt$\cdots CO_2$ complex. In pn systems, ΔE_{ad1}, ΔE_{ad2} and ΔE_{ad3} correspond to CO_2 adsorption energies at N1, N2 and N3 atoms, respectively. The data presented in Tables 1 and 2 suggest that the combined effect of N$\cdots CO_2$ and $CO_2\cdots HO$ interactions result in nearly equivalent CO_2 adsorption strength across N1, N2 and N3 in all Nhet systems. The interaction energy for the first CO_2 adsorption is approximately −10.5 kcal mol^{-1}, for the second CO_2 adsorption is −10.1 kcal mol^{-1}, and for the third CO_2 adsorption is −8.8 kcal mol^{-1}. Moreover, each stage of the CO_2 adsorption

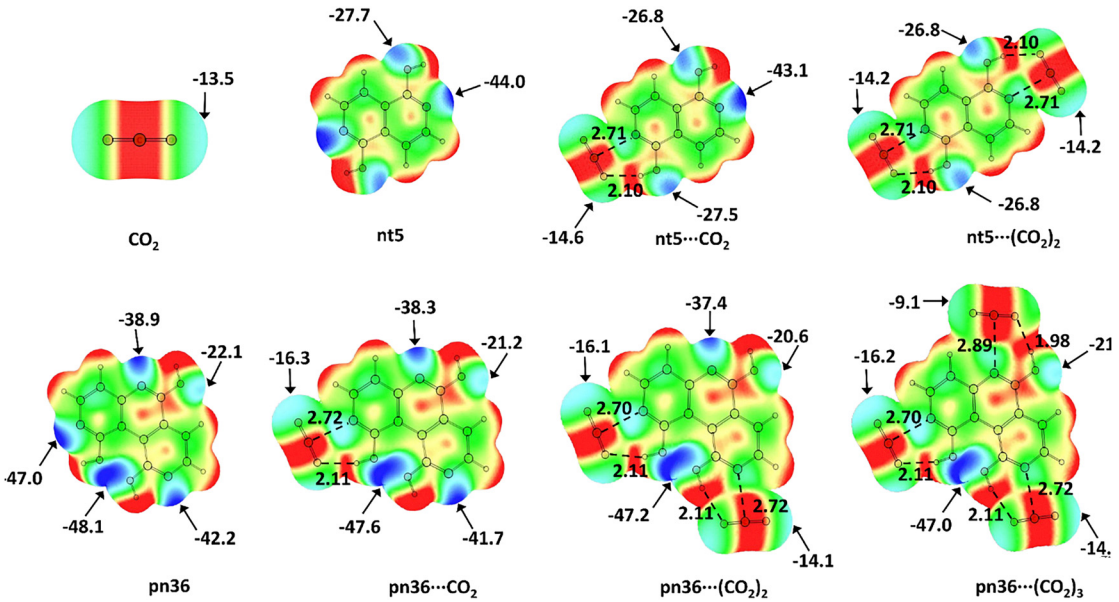

Fig. 3 MESP on 0.005 a.u. isodensity surface for CO_2, N-heterocycles and CO_2 complexes of N-heterocycles. V_{min} values (kcal mol^{-1}), N···CO_2 (d_{NC}) and CO_2···HO (d_{OH}) distances (Å) at M06-2X/6-311++G(d,p) level of theory. Colour code: blue (electron-rich) to red (electron-deficient).

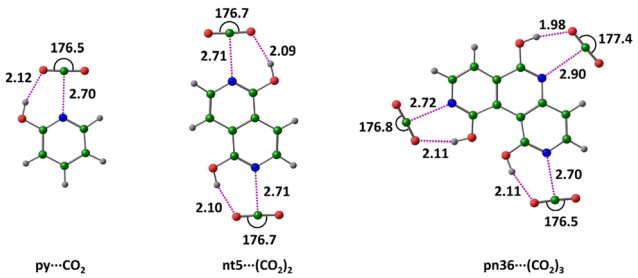

Fig. 4 Optimized structures of Nhet···$(CO_2)_n$ complexes at M06-2X/6-311++G(d,p) level of theory, with bond distances in Å and bond angle in degrees. (Color key: green-C, grey-H, blue-N, red-O).

is exergonic, with average ΔG_{ad1}, ΔG_{ad2} and ΔG_{ad3} values of −3.5, −3.4 and −3.0 kcal mol^{-1}, respectively (Tables 1 and 2). These thermodynamic data confirm that the CO_2 adsorption capacity of naphthyridine is nearly double that of hydroxypyridine, while that of pyridonaphthyridine is nearly triple.

The CO_2···HO hydrogen bond interaction in Nhet···CO_2 can lead to a proton transfer, potentially converting the adsorbed CO_2 into a carboxylate functionality. In other words, the CO_2···HO–C interaction can transition to a CO_2H···O=C interaction, corresponding to an enol–keto transformation of the Nhet system. The schematic representation of CO_2 complex formation and enol–keto transformation is illustrated in Fig. 5 for a representative pn5 system. This transformation simultaneously alters the N···CO_2 noncovalent interaction into a covalent N–CO_2H bond. However, the enol–keto transformation is expected to be energetically unfavourable, as it significantly disrupts the π-electron distribution within the ring, eliminating the alternating single and double bond pattern necessary for aromatic stabilization. In Fig. 5, the regions with reduced aromatic character are highlighted in red. When one hydroxy group is converted to the keto form, the nt moiety is denoted as nt′, while the notation nt″ represents the conversion of both hydroxy groups to the keto form. Similarly, py′ refers to the keto form of hydroxypyridine, while pn′, pn″, and pn‴ represent the keto forms of pyridonaphthyridines.

Although transformation of py···CO_2 to py′-COOH is exothermic by −2.9 kcal mol^{-1}, it is endergonic by 7.8 kcal mol^{-1}, indicating that py′-COOH formation is highly unlikely due to the loss of aromaticity in the ring structure. This trend is consistently observed across most nt and pn systems (Fig. S2, ESI†). In some cases, the formation of carboxylated products is even endothermic. As shown in Fig. 6, the CO_2 adsorption is energetically more favourable than its conversion to carboxylates across all systems due to the partial loss of aromatic character in the keto form. However, certain nt′-COOH and pn′-COOH (the keto forms) exhibit relatively favourable energy values compared to the others. For instance, in nt systems, the formation of nt2′-COOH, nt5′-COOH, nt6′-COOH, nt9′-COOH, and nt10′-COOH is exothermic, while the rest display endothermic behavior. Similarly, among monocarboxylated pn derivatives, pn2′–COOH, pn7′–COOH, pn9′–COOH, pn12′–COOH, pn17′–COOH, pn19′–COOH, pn20′–COOH, pn21′–COOH, pn25′–COOH, pn26′–COOH and pn36′–COOH show better energy data than the rest of the monocarboxylic acids. Compared to pn′–COOH, the relative energy of pn″–$(COOH)_2$ is more negative only in two cases: pn21″–$(COOH)_2$ and pn36″–$(COOH)_2$. In contrast, all tricarboxylated pn‴–$(COOH)_3$ systems have significantly higher energy compared to the corresponding pn···$(CO_2)_3$ complexes. Thus, the energy data presented in Fig. 6 strongly support the efficient capture of CO_2 by Nhet, while its conversion to carboxylates remains energetically demanding due to the loss of aromatic stabilization in the core structure.

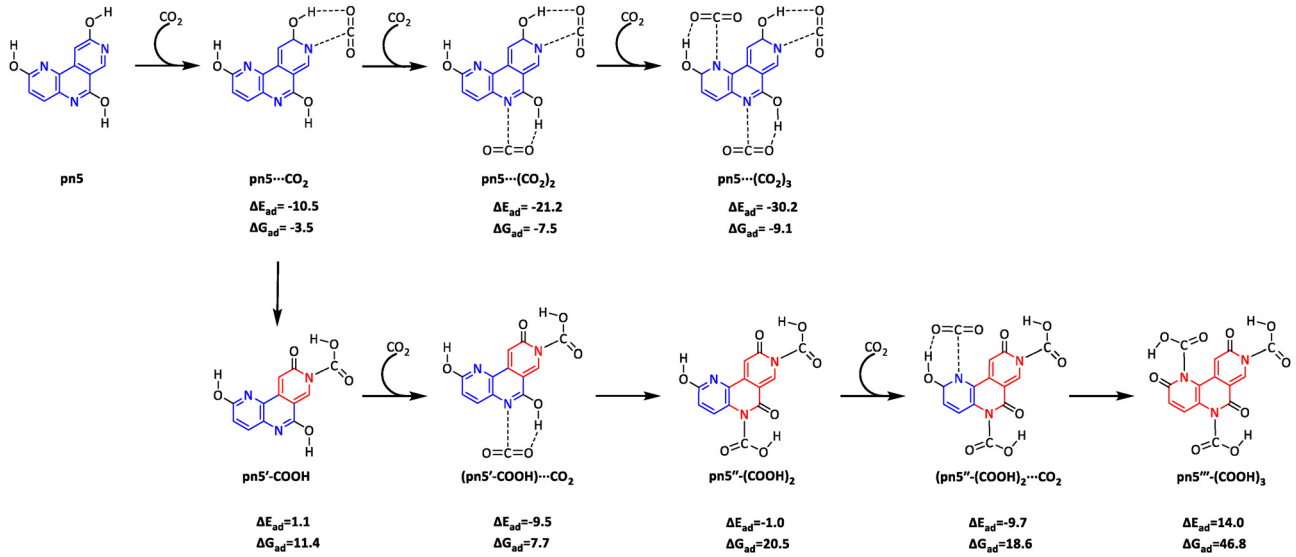

Fig. 5 Schematic illustration of CO_2 complex formation with pn5 and subsequent enol–keto transformations. A ring that cannot be represented by alternate single and double bonds is shown in red.

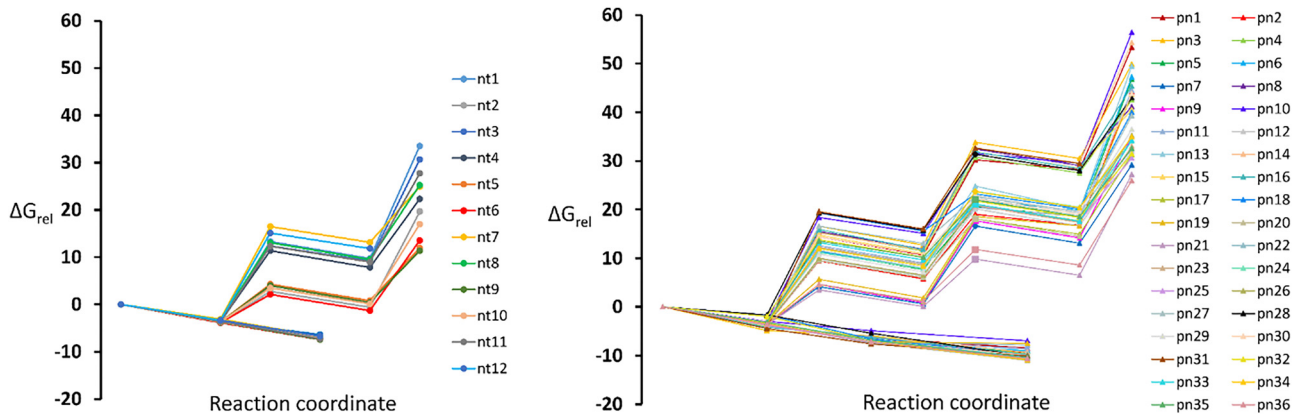

Fig. 6 Relative free energy of the CO_2 complexes of nt and pn molecules. All values in kcal mol^{-1}.

To provide a more thermodynamically meaningful comparison of the different CO_2 adsorption processes, we calculated the relative Gibbs free energies (ΔG_{rel}) for all systems studied. ΔG_{rel} values offer insight into the spontaneity and favourability of each reaction under standard conditions (293 K, 1 atm), incorporating both enthalpic and entropic contributions. These values complement ΔE_{rel} and allow for a more accurate assessment of the adsorption–desorption equilibrium, which is particularly important for evaluating practical CO_2 capture applications (Fig. S2, ESI†). By analyzing ΔG_{rel}, we identify systems where CO_2 binding remains favourable not only in terms of interaction strength but also in terms of thermodynamic feasibility, thereby guiding the selection of optimal candidates for efficient and reversible CO_2 capture.

Interaction of anionic N-heterocycles with CO_2

Luo *et al.* explored the application of pyridine-containing anion-functionalized ionic liquids (ILs) for CO_2 capture.[28] The ILs were synthesized *via* the neutralization of hydroxypyridine using an ethanol solution of trihexyl(tetradecyl)phosphonium hydroxide. Their study proposed a plausible mechanism for CO_2 interaction, identifying the 2-pyridonate ion as the key active species. This ion engages in a two-site interaction with CO_2, where both the oxygen and nitrogen atoms within the anion participate in coordinating and binding CO_2. Building on this mechanism, this study delves into the interaction behavior of the 2-pyridonate ion (py^-) with CO_2. Additionally, as a representative case, the naphthyridonate system ($nt5^-$) is examined to explore the CO_2 adsorption properties of both its monoanionic ($nt5^-$) and dianionic ($nt5^{2-}$) forms. Similarly, for the pyridonaphthyridine system, a representative case, pn36, is selected to investigate the complexation behaviour of its monoanionic ($pn36^-$), dianionic ($pn36^{2-}$) and trianionic ($pn36^{3-}$) forms with CO_2.

Among the various hydroxy-substituted N-heterocycles examined, nt5 and pn36 emerged as the most promising candidates for CO_2 capture based on their computed

interaction energies. The nt5 system, representing the naphthyridine class, demonstrated the highest CO_2 adsorption energy among the twelve derivatives studied, suggesting a strong and favourable interaction with CO_2. Similarly, pn36, a trihydroxy-substituted pyridonaphthyridine, exhibited superior CO_2 binding performance compared to its analogues. These results highlight the importance of both the number and position of hydroxy groups relative to nitrogen centres in facilitating cooperative binding effects. Consequently, nt5 and pn36 were selected for detailed analysis in their anionic forms to further explore the impact of charge and substitution patterns on CO_2 adsorption efficiency.

Fig. 7 illustrates the MESP characteristics of these anions. The MESP minimum (V_{min}) in the vicinity of oxygen atom is consistently more negative than that near than the nitrogen centre. Relative to their neutral counterparts, the monoanions exhibit a significant increase in the magnitude of V_{min}, specifically by 134.0.0, 122.5 and 113.1 kcal mol^{-1}, respectively for py$^-$, nt$^-$, and pn$^-$, respectively. Similarly, the dianions exhibit even more negative V_{min} values than monoanions, with increases of 76.4 and 83.2 kcal mol^{-1} for nt^{2-}and pn^{2-}, respectively. The V_{min} of pn^{3-} is 79.5 kcal mol^{-1} more negative than that of pn^{2-}. This data suggests that the electron-donating interactive behavior of these anionic systems with CO_2 follows the order: trianion > dianion > monoanion » neutral.

The complexation of py$^-$ with CO_2 is more stable when CO_2 binds *via* the nitrogen centre rather than the oxygen centre, with a stability difference of 0.9 kcal mol^{-1}. In both cases, CO_2 forms a covalent bond, as indicated by N–CO_2 and O–CO_2 bond distances within the covalent range. The nitrogen-bound covalent complex $(py–CO_2^-)_N$ and the oxygen-bound covalent complex $(py–CO_2^-)_O$ (Fig. 8) were further analysed for interactions with a second CO_2 molecule. In the scenario where one CO_2 binds at nitrogen and the second at oxygen, the total interaction energy (ΔE_{ad}) is −26.9 kcal mol^{-1}. This complex is denoted as $(py\cdots(CO_2^-)_2)_{N\&O}$ wherein the dotted line indicates that CO_2 molecules are connected noncovalently to N and O. In the case of $(py–CO_2^-)_O$, the second CO_2 interacts noncovalently with the oxygen of the already covalently bound CO_2. This complex $(py–CO_2^-)_O\cdots CO_2$. A similar structure, $(py–CO_2^-)_N\cdots CO_2$ is also identified. Among the complexes the two-CO_2 complexes, the most stable configuration is $(py–CO_2^-)_N\cdots CO_2$ with an ΔE_{ad} of −31.4 kcal mol^{-1}.

For the nt5$^-$ anion, the nitrogen-bound (covalent) complex $(nt5–CO_2^-)_N$ exhibits an ΔE_{ad} of −13.6 kcal mol^{-1}, which is 1.5 kcal mol^{-1} more stable than the oxygen-bound (noncovalent) complex $(nt5^-\cdots CO_2)_O$. Notably, an oxygen-bound covalent complex is not observed. When two CO_2 molecules are adsorbed, one binds covalently to nitrogen while the other interacts noncovalently with oxygen, forming the complex $(CO_2\cdots nt5–CO_2^-)_{N\&O}$, with an ΔE_{ad} of −29.4 kcal mol^{-1}. Another identified structure, $(nt5–CO_2^-)_N\cdots CO_2$ describes the interaction of the second CO_2 with the oxygen of the initially adsorbed CO_2 molecule (Fig. 9).

For the nt5^{2-} dianion interacting with two CO_2 molecules, among the various optimized structures (Fig. S3, ESI†), the most stable configuration is $(nt5–(CO_2^-)_2)_{N\&N}$. Here, both CO_2 molecules form covalent bonds with nitrogen, acquiring carboxylate character and delocalization of the excess negative charge. The ΔE_{ad} of this complex is −59.3 kcal mol^{-1}, meaning the interaction energy per CO_2 molecule adsorbed is −29.7 kcal mol^{-1}-more than twice that of the nt5$^-$ anion and nearly three times that of neutral systems. Further CO_2

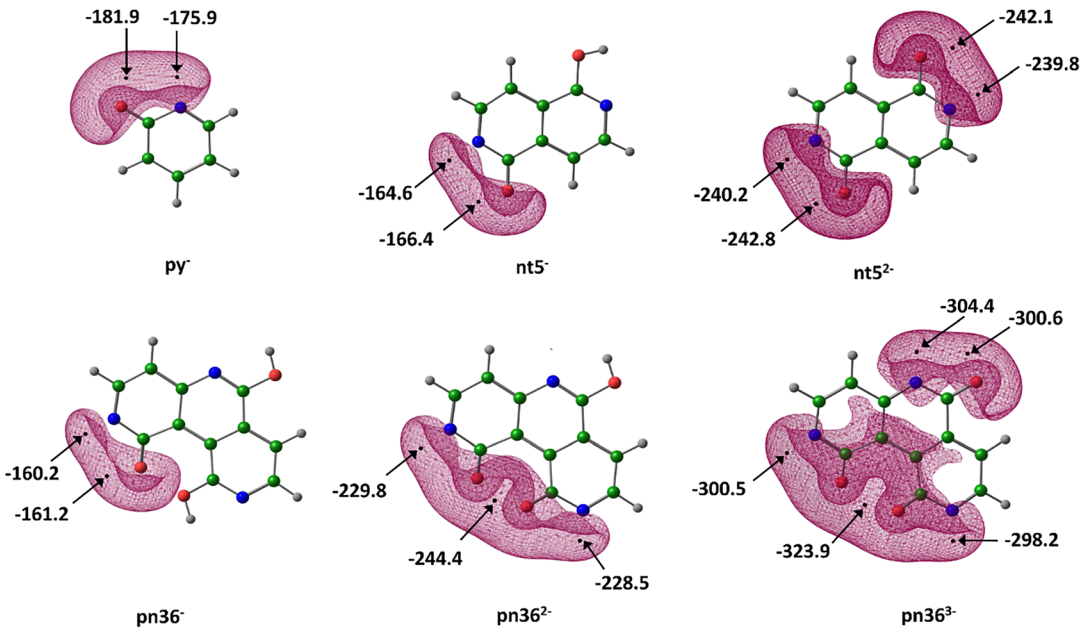

Fig. 7 MESP isosurface at −125.0 kcal mol^{-1} for anions, at −190.0 kcal mol^{-1} for dianions and at −250.0 kcal mol^{-1} for trianion. The location of the MESP minimum point (V_{min}) is shown with black dot and also the corresponding V_{min} value is depicted. (Color key: green-C, grey-H, blue-N, red-O).

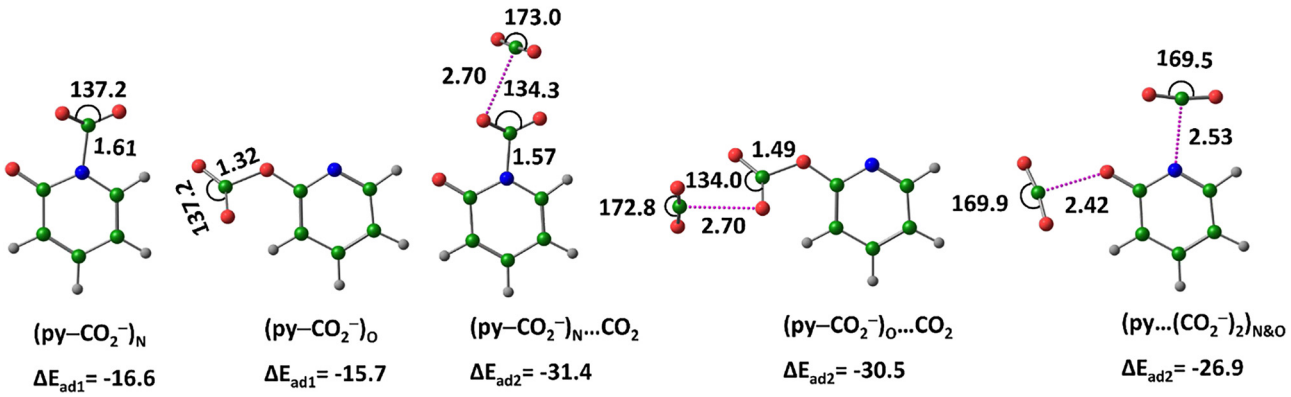

Fig. 8 Optimized structures of the CO_2–adsorbed by py^-, at M06-2X/6-311++G(d,p) level of theory. Distances in Å and angles in degrees. (Color key: green-C, grey-H, blue-N, red-O).

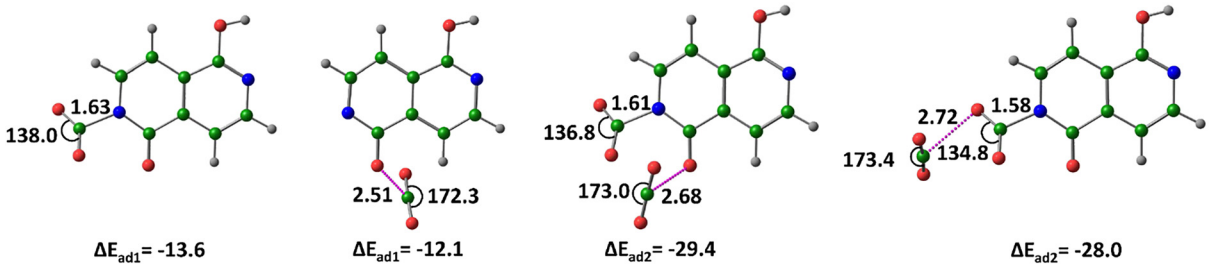

Fig. 9 Optimized structures of the CO_2–adsorbed by $nt5^-$, at M06-2X/6-311++G(d,p) level of theory. Distances in Å and angles in degrees. (Color key: green-C, grey-H, blue-N, red-O).

adsorption occurs *via* an oxygen connection (noncovalent), forming $(CO_2\cdots nt5\text{–}(CO_2^-)_2)_{N\&N\&O}$, which stabilizes the system by an additional 17.7 kcal mol^{-1} (Fig. 10).

For the $pn36^-$ anion, the oxygen-bound (noncovalent) complex $(pn36\cdots CO_2^-)_O$ is slightly more stable than the nitrogen-bound (covalent) complex $(pn36\text{–}CO_2^-)_N$ (Fig. S4, ESI†). However, the most stable configuration with two CO_2 molecules originates from $(\mathbf{pn36}\text{–}CO_2^-)_N$. The complex $(pn36\text{–}CO_2^-)_N\cdots CO_2$, where a second CO_2 interacts with the oxygen of the first adsorbed CO_2, has an energy of −29.4 kcal mol^{-1}-more than twice the interaction energy of $(pn36\text{–}CO_2^-)_N$, indicating strong positive cooperativity.

For the $pn36^{2-}$ dianion, the nitrogen-bound (covalent) CO_2 complex $(pn36^-\text{–}CO_2^-)_N$ is more stable than the oxygen-bound (covalent) complex $(pn36^-\text{–}CO_2^-)_O$ by 8.8 kcal mol^{-1} (Fig. S5, ESI†). The most stable configuration for two $pn36^{2-}$ dianion with two CO_2 molecules is $(pn36\text{–}(CO_2^-)_2)_{N\&N}$, with an ΔE_{ad} of −50.0 kcal mol^{-1}, meaning that the ΔE_{ad} per CO_2 molecule adsorbed is −25.0 kcal mol^{-1}-approximately 12.0 kcal mol^{-1} higher than that of the monoanion. When a third CO_2 molecule is adsorbed through an oxygen connection (noncovalent), forming $(CO_2\cdots pn36\text{–}(CO_2^-)_2)_{N\&N\&O}$, the interaction energy further improves by 17.6 kcal mol^{-1} (Fig. 11).

For the $pn36^{3-}$ trianion, the nitrogen-bound (covalent) CO_2 complex $(pn36^{2-}\text{–}CO_2^-)_N$, is the most stable among all configurations, with ΔE_{ad} = −46.1 kcal mol^{-1} (Fig. 12). Similarly, the nitrogen-bound (covalent) complex with two CO_2 molecules, $(pn36^-\text{–}(CO_2^-)_2)_{N\&N}$, shows the highest stability with

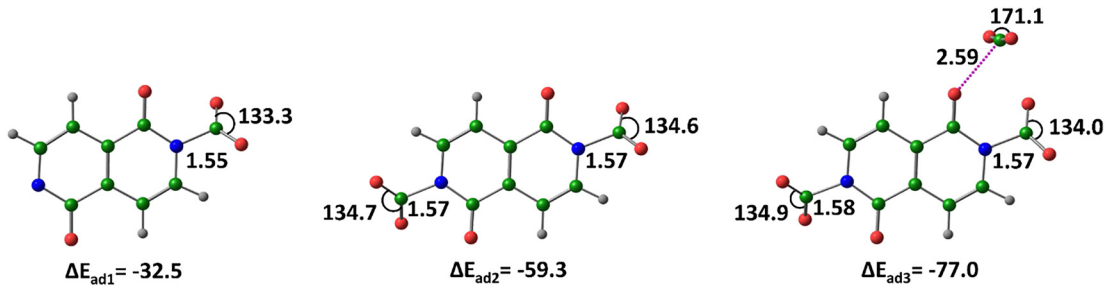

Fig. 10 Optimized structures of the CO_2-adsorbed by $nt5^{2-}$, at M06-2X/6-311++G(d,p) level of theory. Distances in Å and angles in degrees. (Color key: green-C, grey-H, blue-N, red-O).

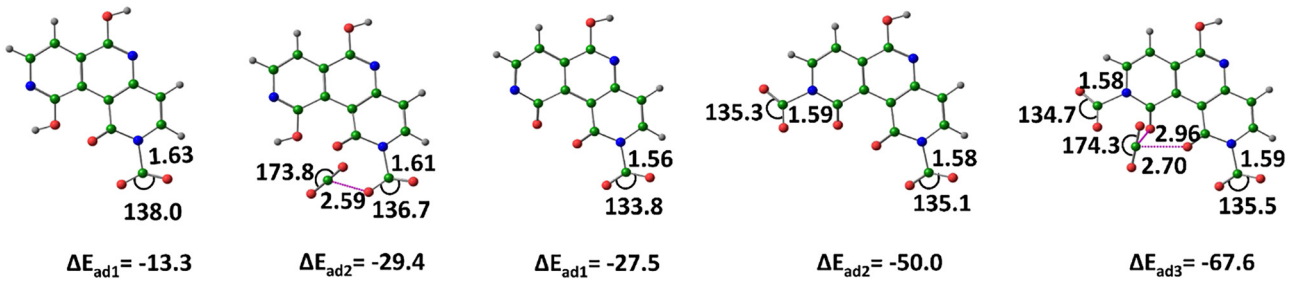

Fig. 11 Optimized structures of the CO_2-adsorbed by $pn36^{-}$ and $pn36^{2-}$, at M06-2X/6-311++G(d,p) level of theory. Distances in Å and angles in degrees. (Color key: green-C, grey-H, blue-N, red-O).

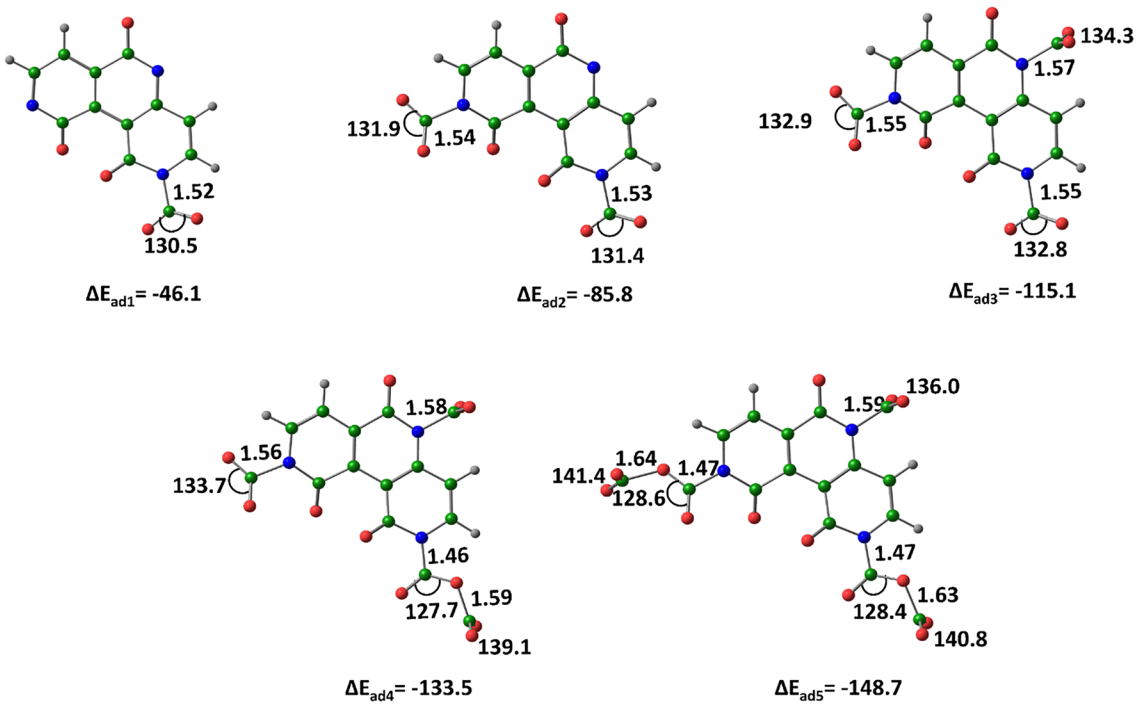

Fig. 12 Optimized structures of the CO_2–adsorbed by $pn36^{3-}$, at M06-2X/6-311++G(d,p) level of theory. Distances in Å and angles in degrees. (Color key: green-C, grey-H, blue-N, red-O).

ΔE_{ad} = −85.8 kcal mol^{-1}. Furthermore, when three CO_2 molecules are adsorbed in a nitrogen-connected (covalent) manner, forming $(pn36\text{–}(CO_2^{-})_3)_{N\&N\&N}$, the ΔE_{ad} reaches −115.1 kcal mol^{-1}, indicating that interaction energy per CO_2 molecule adsorbed is −38.4 kcal mol^{-1}.

Across all anionic, dianionic, and trianionic species, the CO_2 adsorption preferentially occurs at nitrogen rather than oxygen, except in one case (Tables S4 and S5, ESI†). Unlike neutral systems, where N to CO_2 interactions are noncovalent, the anionic systems exhibit covalent N–CO_2 bonding. For dianions, the interaction energy nearly doubles with the adsorption of two CO_2 molecules, while for trianions, it almost triples with three CO_2 molecules. In all cases, carboxylate formation facilitates charge delocalization, centralizing the anionic charge within carboxylate groups, which in turn promotes further CO_2 interactions. As a result, multiple CO_2 molecules are effectively adsorbed, demonstrating significantly enhanced CO_2-binding affinity for anionic species compared to their neutral counterparts. With increasing anionic charge, a substantial increase in ΔE_{ad} is observed, with the trianionic system exhibiting the highest interaction energy. Notably, exergonic CO_2 adsorption involving up to five CO_2 molecules is reported here (Fig. 13 and Table 3). The exergonic nature of these systems is further confirmed by the calculated free energies (Table S6, ESI†).

To assess the practical relevance of CO_2 capture, we computed the CO_2 uptake in terms of weight percent (wt%) using the molar mass ratio of adsorbed CO_2 to the to the total mass of the anion–CO_2 complex (Table S9, ESI†). The calculated values reveal substantial uptake across all anionic systems studied. For instance, the anion of 2-hydroxypyridine captures up to 48% CO_2 by mass with two CO_2 molecules, while the dianion of dihydroxy naphthyridine reaches 45% with three. The trianion of trihydroxy pyridonaphthyridine exhibits the highest uptake, achieving nearly 49 wt% upon binding five CO_2 molecules.

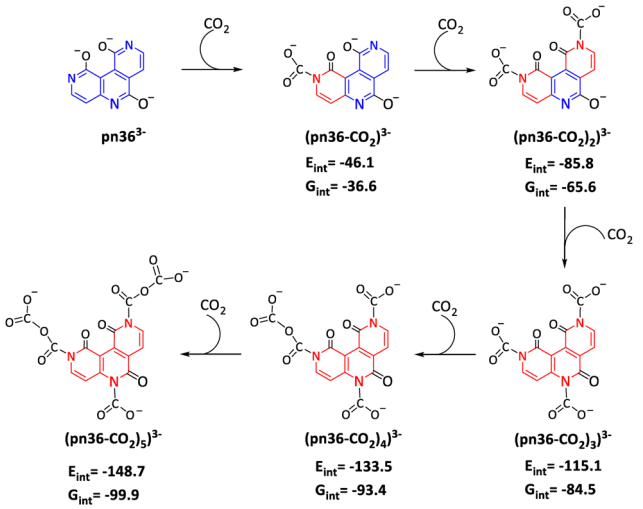

Fig. 13 Schematic illustration of CO_2 complex formation with pn36 trianion. A ring that cannot be represented by alternate single and double bonds is shown in red.

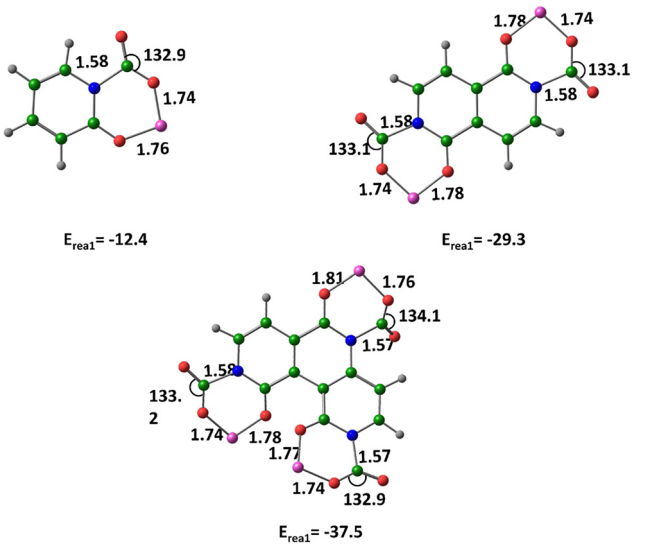

Fig. 14 Optimized structures of CO_2 complexes of Li^+-incorporated anionic systems at M06-2X/6-311++G(d,p) level of theory. Distances in Å and E_{rea1} in kcal mol^{-1}. (Color key: green-C, grey-H, blue-N, red-O, pink-Li).

Table 3 ΔE_{ad} values of selected anions at M06-2X/6-311++G(d,p) level of theory. All values in kcal mol^{-1}

Molecule	ΔE_{ad1}	ΔE_{ad2}	ΔE_{ad3}	ΔE_{ad4}	ΔE_{ad5}
py$^-$	−16.6				
nt5$^-$	−13.6				
nt5^{2-}	−32.5	−59.3			
pn36$^-$	−13.3				
pn36^{2-}	−27.5	−50.0			
pn36^{3-}	−46.1	−85.8	−115.1	−133.5	−148.7

These results underscore the strong potential of these N-heterocyclic systems as high-capacity CO_2 adsorbents.

Influence of counter cations on CO_2 adsorption

To evaluate the impact of counter cations on CO_2 adsorption, the py, nt, and pn systems were studied in the presence of lithium chloride (LiCl), leading to the formation of Li^+-incorporated complexes and HCl (Scheme 1). In these reactions, CO_2 forms nitrogen-bound (covalent) complexes (Fig. 14), which are further stabilized by bidentate Li···O interactions involving both the oxygen of the adsorbent system and the oxygen of the adsorbed CO_2. The energy of reactions (E_{rea1}) given in Scheme 1 was calculated using the equation (eqn (4)):

$$E_{rea1} = \Sigma E_{products} - \Sigma E_{reactants} \quad (4)$$

The E_{rea1} serves as a measure of the adsorption efficiency in the presence of Li^+. These reactions are exothermic, with E_{rea1} values of −12.4, −29.3, and −37.5 kcal mol^{-1}, indicating that, compared to neutral systems, the presence of Li^+ significantly enhances covalent CO_2 binding.

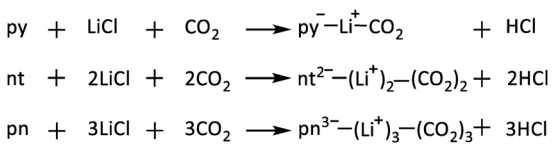

Scheme 1 Reaction of N-heterocycle with LiCl and CO_2.

To further investigate the effect of a larger countercation on CO_2 adsorption, tetramethylphosphonium hydroxide ($(CH_3)_4P^+(OH)^-$) was selected as a model for the bulky trihexyl(tetradecyl)phosphonium hydroxide used by Luo *et al.*[28] Table 4 presents the reaction energies for $(CH_3)_4P^+(OH)^-$ with py, nt, and pn molecules both in the absence and presence of CO_2. The reaction energy (E_{rea3}) in the presence of CO_2 (entries 7–12 in Table 4) is significantly more favourable than in its absence (E_{rea2}; entries 1–6). In both cases, the Gibbs free energy of reaction (G_{rea2} and G_{rea3}) confirms exergonic behaviour. The enhancement of E_{rea3} compared to E_{rea2} (by 40–80%) highlights the strong positive influence of the large counter cation on CO_2 adsorption. The structural analysis of cation-incorporated complexes indicates covalent CO_2 binding at the nitrogen centre (Fig. 15). The acquired anionic character of CO_2 in these complexes leads to stabilizing electrostatic interactions with the surrounding cation. Notably, E_{rea3} improves in the order: complexes with three CO_2 > complexes with two CO_2 > complexes with one CO_2, suggesting that CO_2 adsorption efficiency follows the trend pn > nt > py.

Solvation effect and Gibbs free energy changes

For neutral and anionic Nhet species such as hydroxypyridine (py), dihydroxy naphthyridines (nt), and trihydroxy pyrido-naphthyridines (pn), solvation generally led to a modest reduction in the CO_2 adsorption energies (ΔE_{ad}). This reflects the stabilizing influence of the polar solvent on individual charged and polar components (Table S10, ESI†). For example, the strength of CO_2 adsorption in py weakened with ΔE_{ad} shifting from −10.8 kcal mol^{-1} in the gas phase to −7.6 kcal mol^{-1} in MEA. Similar reductions were observed across nt and pn systems (*e.g.*, ΔE_{ad} for nt5 changed from −10.3 to −7.0 kcal mol^{-1}). As a

Table 4 E_{rea} and G_{rea} values of selected anions with and without CO_2 in the presence of counter cation at M06-2X/6-311++G(d,p) level of theory. All values in kcal mol^{-1}

No.	Reaction	E_{rea2} (1–6) / E_{rea3} (7–12)	G_{rea2} (1–6) / G_{rea3} (7–12)
1	$py + (CH_3)_4P^+(OH)^- \rightarrow py^-\cdots{}^+P(CH_3)_4 + H_2O$	−24.9	−22.8
2	$nt5 + (CH_3)_4P^+(OH)^- \rightarrow nt5^-\cdots{}^+P(CH_3)_4 + H_2O$	−24.5	−23.8
3	$pn36 + (CH_3)_4P^+(OH)^- \rightarrow pn36^-\cdots{}^+P(CH_3)_4 + H_2O$	−24.3	−23.5
4	$nt5 + 2(CH_3)_4P^+(OH)^- \rightarrow nt5^{2-}\cdots{}^+(P(CH_3)_4)_2 + 2H_2O$	−42.8	−39.2
5	$pn36 + 2(CH_3)_4P^+(OH)^- \rightarrow pn36^{2-}\cdots{}^+(P(CH_3)_4)_2 + 2H_2O$	−56.2	−52.7
6	$pn36 + 3(CH_3)_4P^+(OH)^- \rightarrow pn36^{3-}\cdots{}^+(P(CH_3)_4)_3 + 3H_2O$	−72.7	−69.9
7	$py + (CH_3)_4P^+(OH)^- + CO_2 \rightarrow py\text{–}(CO_2)^-\cdots{}^+P(CH_3)_4 + H_2O$	−37.1	−24.6
8	$nt5 + (CH_3)_4P^+(OH)^- + CO_2 \rightarrow nt5\text{–}(CO_2)^-\cdots{}^+P(CH_3)_4 + H_2O$	−41.6	−29.6
9	$pn36 + (CH_3)_4P^+(OH)^- + CO_2 \rightarrow pn36\text{–}(CO_2)^-\cdots{}^+P(CH_3)_4 + H_2O$	−41.6	−29.3
10	$nt5 + 2(CH_3)_4P^+(OH)^- + 2CO_2 \rightarrow (nt5\text{–}(CO_2)_2)^{2-}\cdots{}^+(P(CH_3)_4)_2 + 2H_2O$	−80.7	−56.7
11	$pn36 + 2(CH_3)_4P^+(OH)^- + 2CO_2 \rightarrow (pn36\text{–}(CO_2)_2)^{2-}\cdots{}^+(P(CH_3)_4)_2 + 2H_2O$	−78.9	−55.0
12	$pn36 + 3(CH_3)_4P^+(OH)^- + 3CO_2 \rightarrow (pn36\text{–}(CO_2)_3)^{3-}\cdots{}^+(P(CH_3)_4)_3 + 3H_2O$	−116.9	−79.8

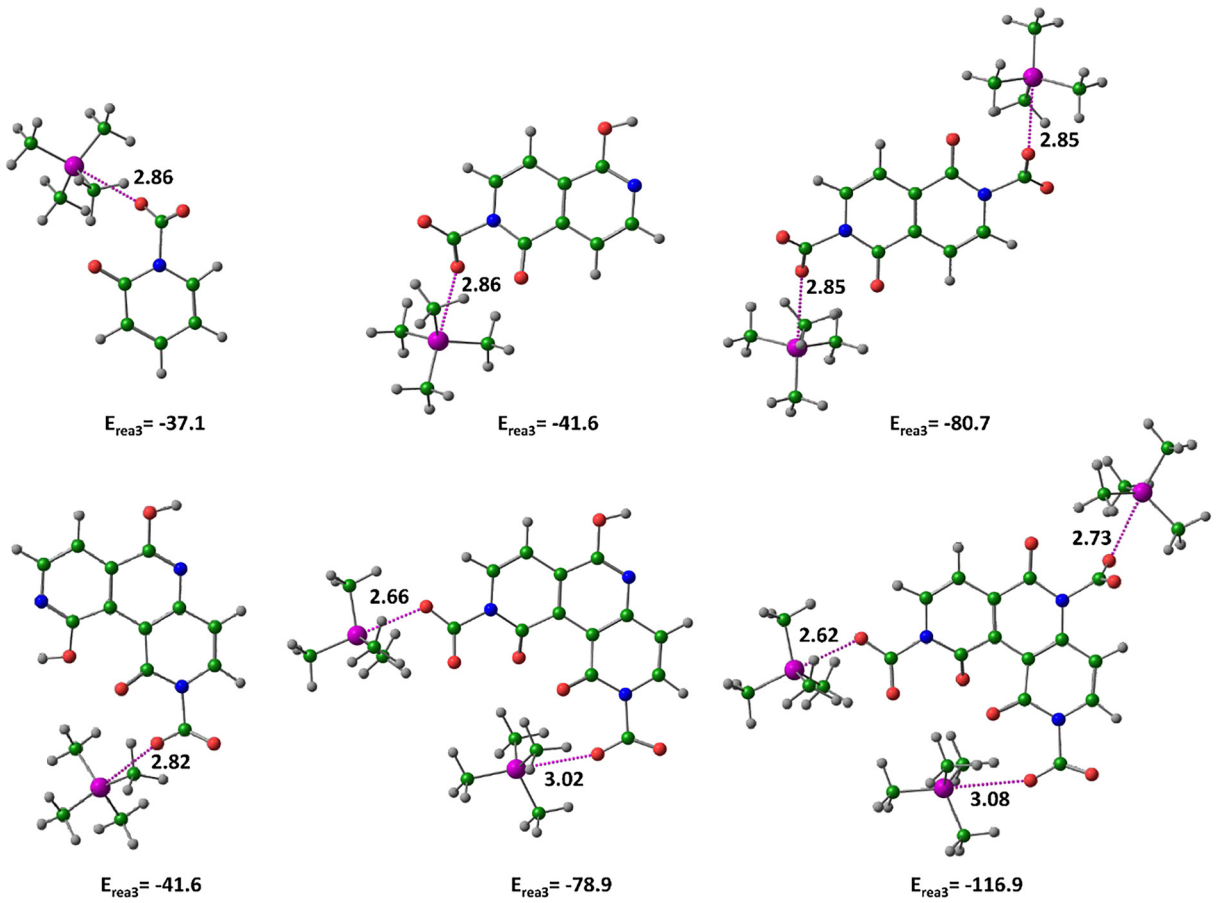

Fig. 15 CO_2 complexes of anionic N-heterocycles in the presence of trimethyl phosphonium cation. Distances in Å. (Color key: green-C, grey-H, blue-N, red-O, magenta-P).

result, the Gibbs free energy of adsorption (ΔG_{ad}) in the solvent phase hovered around thermoneutrality, ranging from −1.6 to +3.2 kcal mol^{-1} for all Nhet$\cdots(CO_2)_n$ complexes (Table S13, ESI†). For anionic species, ΔG_{ad} values were more favourable, falling between −8.7 and 0.1 kcal mol^{-1}, while dianionic systems exhibited ΔG_{ad} values in the range of −23.4 to −1.8 kcal mol^{-1} (Tables S14 and S15, ESI†). Notably, trianions showed the most exergonic adsorption, with ΔG_{ad} values between −26.3 and −7.8 kcal mol^{-1} (Table S16, ESI†).

In comparison to the gas phase, a substantial reduction (71–81%) of the reaction energy (E_{rea1}) is observed in the solvent phase for the reactions described in Scheme 1, which involve the formation of CO_2 complexes of Nhet in the presence of Li^+. A similar trend is noted for the formation of ion pairs between

Nhet and the bulky cation $(CH_3)_4P^+(OH)^-$ with a marked reduction in exothermicity (E_{rea2}) in solution—by 52% for py, and more modest reductions for nt (16%) and pn (6%) systems (entries 1–6, Table 4). These observations are consistent with the strong solvation of the small, highly charged Li^+ ion, which stabilizes the free cation more than the associated complex, thereby lowering the net driving force for complexation. In contrast, the bulky cation $(CH_3)_4P^+(OH)^-$ is less strongly solvated due to its diffuse charge distribution, resulting in a smaller energetic penalty upon complex formation. The nt and pn systems may further resist tight ion pairing due to steric or electronic factors, contributing to the relatively lower impact of solvation.

Interestingly, a moderate enhancement (6–9%) in exothermic character (E_{rea3}) is observed in the solvent phase for the formation of CO_2 complexes from pre-formed Nhet$\cdots(CH_3)_4P^+(OH)^-$ ion pairs (entries 7–12, Table 4). This likely arises from solvent-induced weakening of the cation–anion interaction, which renders the anion more accessible for CO_2 binding, thereby enhancing the overall adsorption energy in the solvated environment. The corresponding Gibbs free energies of reaction G_{rea3} in solution range from -26.8 kcal mol^{-1} for the monoanionic complex py–$(CO_2)^-\cdots{}^+P(CH_3)_4$ to -81.2 kcal mol^{-1} for the trianionic complex $(pn–(CO_2)_3)^{3-}\cdots{}^+(P(CH_3)_4)_3$.

The strongly negative ΔG_{ad} values observed in solution for many dianionic and trianionic systems along with the highly exergonic character of G_{rea3} suggest that these Nhet-based framework systems have the potential to bind more CO_2 molecules than currently explored. These findings highlight the promising CO_2 uptake capacity of such systems and underscore the critical role of solvation in modulating both the thermodynamics and the cooperative effects involved in CO_2 capture. They emphasize that solvent-specific interactions must be carefully considered in the rational design of efficient and regenerable CO_2 adsorbents for solution-phase applications.

Conclusions

This comprehensive DFT study highlights the exceptional CO_2 capture capabilities of hydroxy-substituted aromatic N-heterocycles, revealing their potential as powerful adsorbents for mitigating greenhouse gas emissions. Through density functional theory (DFT) calculations, we have demonstrated that strategic incorporation of nitrogen and hydroxy groups within the molecular structures of pyridines, naphthyridines, and pyridonaphthyridines fosters cooperative binding mechanisms, leading to enhanced CO_2 adsorption. The findings reveal that the adsorption CO_2 capacity increases with the number of nitrogen and hydroxy centres.

A key breakthrough in this study is the significantly enhanced CO_2 adsorption observed in the anionic forms of these N-heterocycles. Compared to their neutral counterparts, anionic species exhibit significantly stronger CO_2 interactions, with the formation of covalent bonds between nitrogen and CO_2. As the anionic charge increases from monoanion to dianion and trianion, the CO_2-binding affinity improves dramatically due to charge delocalization, resulting in more exergonic adsorption energies. This trend suggests that designing anionic or negatively charged frameworks could be an effective strategy for developing highly efficient CO_2 capture materials. Importantly, solvation effects modeled using monoethanolamine (MEA) show that while polar solvents modestly reduce adsorption energies in neutral and anionic systems, they can enhance CO_2 binding in ion-paired complexes by disrupting ion-pairing and increasing CO_2 accessibility.

Energetic analysis further supports these findings, showing that CO_2 adsorption is generally exergonic under post-combustion conditions (293 K, 1 atm). Notably, the interaction energy per CO_2 molecule in trianionic species is nearly three times higher than in neutral systems, underscoring the role of charge modulation in enhancing CO_2 capture efficiency. The study also establishes that enol–keto transformations, which could potentially convert the adsorbed CO_2 into carboxylate groups, are energetically unfavourable. This is attributed to the loss of aromaticity in the core structure of N-heterocycles, reinforcing the importance of preserving aromatic stability for maintaining efficient CO_2 adsorption.

Additionally, the influence of counter cations, such as lithium and tetramethylphosphonium, in stabilizing CO_2 adsorption has been explored. The presence of these cations further strengthens CO_2 binding by reducing interaction distances and increasing exergonicity, thereby improving the overall adsorption performance. These results suggest that incorporating appropriate cations into CO_2 capture materials could enhance their efficiency, offering another avenue for material optimization.

Overall, this study provides valuable molecular-level insights into the structure–activity relationships governing CO_2 capture in hydroxy-substituted N-heterocycles. The findings suggest that these molecules, particularly in their anionic and cation-stabilized forms, hold significant promise for developing next-generation CO_2 capture technologies. Future research should focus on experimentally validating these computational predictions and exploring the practical implementation of these materials under real-world conditions. Furthermore, extending this approach to solid-state frameworks, such as functionalized porous materials or ionic liquids, could offer additional pathways for enhancing CO_2 capture efficiency and selectivity.

Author contributions

CHS conceptualized the project, supervised the work, and contributed to the writing of the manuscript. PKA conducted research, curated the data, and contributed to the writing of the manuscript.

Conflicts of interest

There are no conflicts to declare.

Data availability

The data supporting this article have been included as part of the ESI.†

Acknowledgements

PKA is thankful to DST, Inspire, for a Senior Research Fellowship. CHS acknowledges CSIR-NIIST, Trivandrum for his deputation assignment as Director to SRIBS, Kottayam.

References

1 E. J. Beckman, *Ind. Eng. Chem. Res.*, 2003, **42**, 1598–1602.
2 D. J. Darensbourg, *Inorg. Chem.*, 2010, **49**, 10765–10780.
3 M. Mikkelsen, M. Jørgensen and F. C. Krebs, *Energy Environ. Sci.*, 2010, **3**, 43–81.
4 K. S. Lackner, *Science*, 2003, **300**, 1677–1678.
5 N. MacDowell, N. Florin, A. Buchard, J. Hallett, A. Galindo, G. Jackson, C. S. Adjiman, C. K. Williams, N. Shah and P. Fennell, *Energy Environ. Sci.*, 2010, **3**, 1645–1669.
6 P. Vadivelu and C. H. Suresh, *Dalton Trans.*, 2015, **44**, 16847–16853.
7 M. J. Ajitha and C. H. Suresh, *Tetrahedron Lett.*, 2011, **52**, 5403–5406.
8 S. Choi, J. H. Drese and C. W. Jones, *ChemSusChem*, 2009, **2**, 796–854.
9 E. S. Rubin, H. Mantripragada, A. Marks, P. Versteeg and J. Kitchin, *Prog. Energy Combust. Sci.*, 2012, **38**, 630–671.
10 M. E. Boot-Handford, J. C. Abanades, E. J. Anthony, M. J. Blunt, S. Brandani, N. Mac Dowell, J. R. Fernández, M.-C. Ferrari, R. Gross and J. P. Hallett, *Energy Environ. Sci.*, 2014, **7**, 130–189.
11 M. Younas, M. Sohail, L. Leong, M. Bashir and S. Sumathi, *Int. J. Environ. Sci. Technol.*, 2016, **13**, 1839–1860.
12 M. Plaza, C. Pevida, A. Arenillas, F. Rubiera and J. Pis, *Fuel*, 2007, **86**, 2204–2212.
13 J. Hack, N. Maeda and D. M. Meier, *ACS Omega*, 2022, **7**, 39520–39530.
14 M. J. Ajitha and C. H. Suresh, *J. Org. Chem.*, 2012, **77**, 1087–1094.
15 S. Anila and C. H. Suresh, *New J. Chem.*, 2023, **47**, 3047–3054.
16 M. J. Muldoon, S. N. Aki, J. L. Anderson, J. K. Dixon and J. F. Brennecke, *J. Phys. Chem. B*, 2007, **111**, 9001–9009.
17 B. E. Gurkan, J. C. de la Fuente, E. M. Mindrup, L. E. Ficke, B. F. Goodrich, E. A. Price, W. F. Schneider and J. F. Brennecke, *J. Am. Chem. Soc.*, 2010, **132**, 2116–2117.
18 Z. Xue, Z. Zhang, J. Han, Y. Chen and T. Mu, *Int. J. Greenhouse Gas Control*, 2011, **5**, 628–633.
19 E. D. Bates, R. D. Mayton, I. Ntai and J. H. Davis, *J. Am. Chem. Soc.*, 2002, **124**, 926–927.
20 I. Niedermaier, M. Bahlmann, C. Papp, C. Kolbeck, W. Wei, S. Krick Calderón, M. Grabau, P. S. Schulz, P. Wasserscheid and H.-P. Steinrück, *J. Am. Chem. Soc.*, 2014, **136**, 436–441.
21 L. G. Sánchez, G. Meindersma and A. De Haan, *J. Chem. Eng.*, 2011, **166**, 1104–1115.
22 P. Sharma, S. Do Park, K. T. Park, S. C. Nam, S. K. Jeong, Y. I. Yoon and I. H. Baek, *J. Chem. Eng.*, 2012, **193**, 267–275.
23 J.-G. Lu, C.-T. Lu, Y. Chen, L. Gao, X. Zhao, H. Zhang and Z.-W. Xu, *Appl. Energy*, 2014, **115**, 573–581.
24 Y. S. Sistla and A. Khanna, *J. Chem. Eng.*, 2015, **273**, 268–276.
25 B. Lv, G. Jing, Y. Qian and Z. Zhou, *J. Chem. Eng.*, 2016, **289**, 212–218.
26 X. Y. Luo, X. Y. Lv, G. L. Shi, Q. Meng, H. R. Li and C. M. Wang, *AIChE J.*, 2019, **65**, 230–238.
27 S. Anila and C. H. Suresh, *Phys. Chem. Chem. Phys.*, 2022, **24**, 22144–22153.
28 X. Luo, Y. Guo, F. Ding, H. Zhao, G. Cui, H. Li and C. Wang, *Angew. Chem., Int. Ed.*, 2014, **126**, 7173–7177.
29 C. Wang, H. Luo, D. E. Jiang, H. Li and S. Dai, *Angew. Chem., Int. Ed.*, 2010, **122**, 6114–6117.
30 X. Y. Luo, F. Ding, W. J. Lin, Y. Q. Qi, H. R. Li and C. M. Wang, *J. Phys. Chem. Lett.*, 2014, **5**, 381–386.
31 C. Wang, X. Luo, H. Luo, D. e Jiang, H. Li and S. Dai, *Angew. Chem., Int. Ed.*, 2011, **21**, 5020–5024.
32 C. Wang, S. M. Mahurin, H. Luo, G. A. Baker, H. Li and S. Dai, *Green Chem.*, 2010, **12**, 870–874.
33 C. Wang, H. Luo, X. Luo, H. Li and S. Dai, *Green Chem.*, 2010, **12**, 2019–2023.
34 Y. Huang, G. Cui, Y. Zhao, H. Wang, Z. Li, S. Dai and J. Wang, *Angew. Chem., Int. Ed.*, 2017, **56**, 13293–13297.
35 X. Luo and C. Wang, *Curr. Opin. Green Sustainable Chem.*, 2017, **3**, 33–38.
36 S. Anila and C. H. Suresh, *Phys. Chem. Chem. Phys.*, 2021, **23**, 13662–13671.
37 S. Anila and C. H. Suresh, *Phys. Chem. Chem. Phys.*, 2019, **21**, 23143–23153.
38 S. Anila, C. H. Suresh and H. F. Schaefer III, *J. Phys. Chem. A*, 2022, **126**, 4952–4961.
39 J. Wang, L. Huang, R. Yang, Z. Zhang, J. Wu, Y. Gao, Q. Wang, D. O'Hare and Z. Zhong, *J. Energy Environ. Sci.*, 2014, **7**, 3478–3518.
40 B. Gurkan, B. Goodrich, E. Mindrup, L. Ficke, M. Massel, S. Seo, T. Senftle, H. Wu, M. Glaser and J. Shah, *J. Phys. Chem. Lett.*, 2010, **1**, 3494–3499.
41 T. Su, T. Lyu, S. Wang, X. Tian, Z. Chen, W. Chu, M. Xie, S. Wang and Y. Zhuo, *Energy Fuels*, 2025, **39**, 1216–1225.
42 M. J. Frisch, G. W. Trucks, H. B. Schlegel, G. E. Scuseria, M. A. Robb, J. R. Cheeseman, G. GScalmani, V. Barone, G. A. Petersson, H. Nakatsuji, X. Li, M. Caricato, A. V. Marenich, J. Bloino, B. G. Janesko, R. Gomperts, B. Mennucci, H. P. Hratchian, J. V. Ortiz, A. F. Izmaylov, J. L. Sonnenberg, D. Williams-Young, F. Ding, F. Lipparini, F. Egidi, J. Goings, B. Peng, A. Petrone, T. Henderson, D. Ranasinghe, V. G. Zakrzewski, J. Gao, N. Rega, G. Zheng, W. Liang, M. Hada, M. Ehara, K. Toyota, R. Fukuda, J. Hasegawa, M. Ishida, T. Nakajima, Y. Honda, O. Kitao, H. Nakai, T. Vreven, K. Throssell, J. A. Montgomery, J. E. Peralta, F. Ogliaro, M. J. Bearpark, J. J. Heyd, E. N. Brothers, K. N. Kudin, V. N. Staroverov, T. A. Keith, R. Kobayashi, J. Normand, K. Raghavachari, A. P. Rendell, J. C. Burant, S. S. Iyengar, J. Tomasi, M. Cossi, J. M. Millam, M. Klene,

C. Adamo, R. Cammi, J. W. Ochterski, R. L. Martin, K. Morokuma, O. Farkas, J. B. Foresman and D. J. Fox, *Gaussian 16, Revision A. 03*, Gaussian, Wallingford, CT, 2016.
43 Y. Zhao and D. G. Truhlar, *Theor. Chem. Acc.*, 2008, **120**, 215–241.
44 S. F. Boys and F. Bernardi, *Mol. Phys.*, 1970, **19**, 553–566.
45 C. Reichardt, *Org. Process Res. Dev.*, 2007, **11**, 105–113.
46 A. J. Reynolds, T. V. Verheyen, S. B. Adeloju, E. Meuleman and P. Feron, *Environ. Sci. Technol.*, 2012, **46**, 3643–3654.
47 A. V. Marenich, C. J. Cramer and D. G. Truhlar, *J. Phys. Chem. B*, 2009, **113**, 6378–6396.
48 P. Politzer and D. G. Truhlar, *Chemical applications of atomic and molecular electrostatic potentials: reactivity, structure, scattering, and energetics of organic, inorganic, and biological systems*, New York, 1981.
49 S. R. Gadre and R. N. Shirsat, *Electrostatics of atoms and molecules*, Hyderabad, 2000.
50 N. Mohan and C. H. Suresh, *J. Phys. Chem. A*, 2014, **118**, 1697–1705.
51 P. V. Bijina and C. H. Suresh, *J. Chem. Sci.*, 2016, **128**, 1677–1686.
52 C. H. Suresh and S. Anila, *Acc. Chem. Res.*, 2023, **56**, 1884–1895.
53 G. R. Newkome, S. J. Garbis, V. K. Majestic, F. R. Fronczek and G. Chiari, *J. Org. Chem.*, 1981, **46**, 833–839.
54 A. M. Thompson, A. M. Delaney, J. M. Hamby, M. C. Schroeder, T. A. Spoon, S. M. Crean, H. H. Showalter and W. A. Denny, *J. Med. Chem.*, 2005, **48**, 4628–4653.
55 A. M. Thompson, G. W. Rewcastle, S. L. Boushelle, B. G. Hartl, A. J. Kraker, G. H. Lu, B. L. Batley, R. L. Panek, H. H. Showalter and W. A. Denny, *J. Med. Chem.*, 2000, **43**, 3134–3147.
56 T. K. Dawson, P. Dziedzic, M. J. Robertson, J. A. Cisneros, S. G. Krimmer, A. S. Newton, J. Tirado-Rives and W. L. Jorgensen, *ACS Med. Chem. Lett.*, 2017, **8**, 1287–1291.
57 H. Natsugari, Y. Ikeura, Y. Kiyota, Y. Ishichi, T. Ishimaru, O. Saga, H. Shirafuji, T. Tanaka and I. Kamo, *J. Med. Chem.*, 1995, **38**, 3106–3120.
58 T. Cailly, F. Fabis, R. Legay, H. Oulyadi and S. Rault, *Tetrahedron*, 2007, **63**, 71–76.
59 Y. Hamada, M. Sato and I. Takeuchi, *J. Pharm. Soc. Jpn.*, 1975, **95**, 1492–1497.
60 H.-J. Fan and C.-W. Liu, *Chem. Phys. Lett.*, 1999, **300**, 351–358.
61 B. Bhargava and S. Balasubramanian, *Chem. Phys. Lett.*, 2007, **444**, 242–246.
62 B. Bhargava, M. Saharay and S. Balasubramanian, *Bull. Mater. Sci.*, 2008, **31**, 327–334.
63 K. M. Gupta and J. Jiang, *J. Phys. Chem. C*, 2014, **118**, 3110–3118.
64 J. X. Mao, J. A. Steckel, F. Yan, N. Dhumal, H. Kim and K. Damodaran, *Phys. Chem. Chem. Phys.*, 2016, **18**, 1911–1917.
65 A. R. Shaikh, H. Karkhanechi, E. Kamio, T. Yoshioka and H. Matsuyama, *J. Phys. Chem. C*, 2016, **120**, 27734–27745.
66 X. Zhang, X. Zhang, H. Dong, Z. Zhao, S. Zhang and Y. Huang, *Energy Environ. Sci.*, 2012, **5**, 6668–6681.
67 A. P. Hallenbeck and J. R. Kitchin, *Eng. Chem. Res.*, 2013, **52**, 10788–10794.
68 J. Wang, L. Huang, R. Yang, Z. Zhang, J. Wu, Y. Gao, Q. Wang, D. O'Hare and Z. Zhong, *Energy Environ. Sci.*, 2014, **7**, 3478–3518.
69 A. Sanna, M. Uibu, G. Caramanna, R. Kuusik and M. Maroto-Valer, *Chem. Soc. Rev.*, 2014, **43**, 8049–8080.
70 A. Goeppert, M. Czaun, J.-P. Jones, G. S. Prakash and G. A. Olah, *Chem. Soc. Rev.*, 2014, **43**, 7995–8048.
71 N. Hollingsworth, S. R. Taylor, M. T. Galante, J. Jacquemin, C. Longo, K. B. Holt, N. H. De Leeuw and C. Hardacre, *Angew. Chem., Int. Ed.*, 2015, **127**, 14370–14374.
72 D. Chen, X. Zhang and A. F. Lee, *J. Mater. Chem. A*, 2015, **3**, 14487–14516.
73 M. Marszewski, S. Cao, J. Yu and M. Jaroniec, *Mater. Horiz.*, 2015, **2**, 261–278.
74 G. A. Ozin, *Adv. Mater.*, 2015, **27**, 1957–1963.
75 J. Kothandaraman, A. Goeppert, M. Czaun, G. A. Olah and G. S. Prakash, *J. Am. Chem. Soc.*, 2016, **138**, 778–781.
76 I. H. Arellano, S. H. Madani, J. Huang and P. Pendleton, *J. Chem. Eng.*, 2016, **283**, 692–702.
77 S. R. Gadre, C. H. Suresh and N. Mohan, *Molecules*, 2021, **26**, 3289.
78 C. H. Suresh, G. S. Remya and P. K. Anjalikrishna, *Wiley Interdiscip. Rev.: Comput. Mol. Sci.*, 2022, **12**, e1601.
79 P. V. Bijina and C. H. Suresh, *J. Phys. Chem. A*, 2020, **124**, 2231–2241.

